Dielectric Barrier Discharge Plasma Actuator Thrust Measurement Methodology Incorporating Antithrust Hypothesis

David E. Ashpis
NASA John H. Glenn Research Center, Cleveland, Ohio 44135
and
Matthew C. Laun
HX5 Sierra, LLC, Cleveland, Ohio 44135

The thrust of the dielectric barrier discharge plasma actuator is the plasma body force minus the wall shear force, and it equals the net induced momentum. Thrust measurement simplicity makes it a good metric of the aerodynamic performance for active flow control applications. Uncertainty and non-repeatability issues with conventional test setups motivated development of a novel suspended actuator test setup and a measurement methodology consisting of a burn-in procedure followed by frequency scans at constant voltages. This approach led to observation of negative values of thrust, or "antithrust," at low frequencies between 4 Hz and up to 64 Hz. The antithrust is proportional to the mean-squared voltage and is frequency independent. Departures from the parabolic antithrust curve are correlated with appearance of visible plasma discharges. The antithrust hypothesis is proposed. It states that the measured thrust is the sum of plasma thrust and antithrust. The magnitude of the antithrust depends on the actuator geometry, the materials, and the test installation. The dependence on test installation was validated by surrounding the actuator with a grounded large-diameter metal sleeve. A thrust data correction for antithrust enables meaningful comparisons between actuators at different installations. A strong dependence on humidity is also shown. The thrust significantly decreases with increasing humidity.

Nomenclature

F	=	frequency
k	=	antithrust coefficient
V	=	mean voltage

Subscripts

p-p, pp	=	peak to peak

I. Introduction

A DIELECTRIC barrier discharge (DBD) actuator is a device that consists of a pair of electrodes separated by a dielectric. One electrode is exposed to the flow and the other is covered. Alternating current (ac) voltage in multiple kilovolt range is applied to the electrodes and creates weakly ionized surface discharge plasma on the exposed electrode edge toward the buried electrode direction (Fig. 1). There are usually two modes of operation. Conventional DBD operation involves application of an ac voltage waveform in the kilohertz frequency range, with or without modulation or pulsing. In this mode, referred to as "AC-DBD," heat generation is insignificant and the actuator generates momentum in the form of a wall jet parallel to the surface. The wall-jet momentum coupling with the external flow is the foundation for active flow control. The other mode of DBD operation involves applying short-duration voltage pulses, on the order of 10–100 ns wide, with a repetition rate range from a few hundred hertz to a few hundred kilohertz. In this mode of operation, generally referred to as "NS-DBD," the generated momentum is usually negligible but there is a fast, localized heating of the gas that creates pressure waves or even shock waves. The repetition generates pressure oscillations that are used for active flow control. For the AC-DBD actuator, see review articles by Moreau [1], Corke et al. [2–4], Benard and Moreau [5], Kotsonis [6], and Kriegseis et al. [7]. For the NS-DBD actuator, see the paper by Roupassov et al. [8]. Combinations of AC-DBD and NS-DBD were also reported by Starikovskiy et al. [9].

This project is limited to the conventional AC-DBD momentum-generating actuator with ac operation and without modulation. The interest is to characterize the aerodynamic performance of the actuator. Generally, it is performed without external flow. This paper is focused on the actuator thrust. It addresses several related issues; and it describes a novel test setup, a new measurement methodology, and data interpretation approaches that have lead to the discovery of negative- or counter-thrust that we termed antithrust. The antithrust hypothesis is proposed, and it is used to provide correction to measured thrust results.

II. Thrust of the DBD Actuator

The DBD actuator induces momentum via the electrohydrodynamic (EHD) effect, which is a collision mechanisms between charged ions and the neutrals. The thrust of the DBD plasma actuator is the reaction force to the induced momentum and therefore can serve as a good metric for its aerodynamic performance. The reason is that, in active flow control applications, the main interest is in the momentum injected into the flow by an actuator. Pneumatic actuators use a momentum coefficient as a performance and characterization parameter (e.g., Glezer and Amitay [10]).

A clear definition of terminology and an understanding of the relationship between thrust and the induced momentum are warranted. We use a control volume in the flow region above the actuator surface, which is shown in Fig. 2a [11]. The EHD effect can be represented as spatiotemporal distribution of volumetric forces $f(x,t)$ inside the control volume. Volume integration yields a time-dependent body force $f(t)$ that can be further time averaged to yield the average plasma force F_p. The induced flow also generates a surface-averaged time-dependent wall shear force $f_s(t)$, and time-averaging yields the wall shear force F_s. Figure 2b shows the forces acting on the actuator plate isolated as a free body, and it includes the reaction to the time-averaged plasma body force F_p, the wall shear force F_s, and the thrust T_x. There

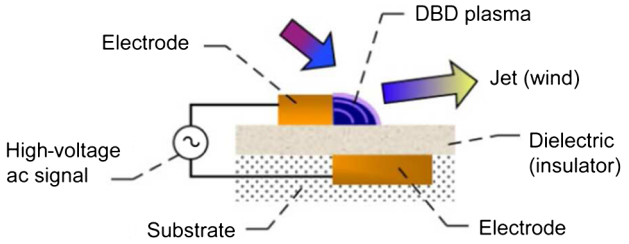

Fig. 1 Schematic of a DBD plasma actuator.

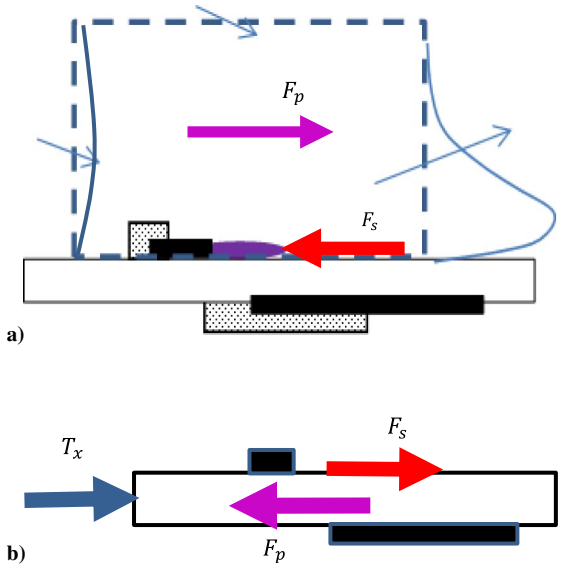

Fig. 2 Representations of a) control volume for thrust evaluation and b) forces on the actuator plate.

is also surface-normal force component, but only the force equilibrium in the streamwise (surface-parallel) direction is of interest, leading to the relationship

$$T_x = F_p - F_s \tag{1}$$

Time-averaged values are used because the thrust T_x can be measured by a force sensing device, which is usually a force balance that has a low-frequency response and measures time-averaged forces. It is clear that the thrust reading of the balance T_x differs from the plasma body force F_p by the magnitude of the wall shear force F_s.

The thrust is equal to the net momentum leaving the control volume (pressure on the left and right faces is equal for the practical range of induced velocities by DBD actuators) [11,12], which is useful information for active flow control applications. However, there is also interest in quantifying the body force F_p because it is responsible for the coupling to the controlled flow. The wall shear force is not necessarily negligible, and the question arises as to what is its magnitude relative to the body force. Durscher and Roy [13] have shown dependence of the thrust on the distance from the edge of the exposed electrode to the edge of the actuator plate. The dependence is weak above a voltage-dependent minimum distance, and the thrust asymptotes to a fairly constant value. They attributed this behavior to wall shear, but they also suspected distance-dependent surface charging as a contributing factor. Opaits et al. [14] found that the induced wall jet obeyed Glauert's similarity wall-jet solution [15]. We complemented [14] by calculating the corresponding wall shear and found it to be negligible (unpublished results). However, close to the exposed electrode, the similarity solution is invalid, and shear stresses cannot be obtained from the similarity solution, leaving the magnitude of the overall wall shear force still in question.

Laser Doppler anemometry (LDA) and particle image velocimetry (PIV) were used by several researcher groups for measuring the DBD

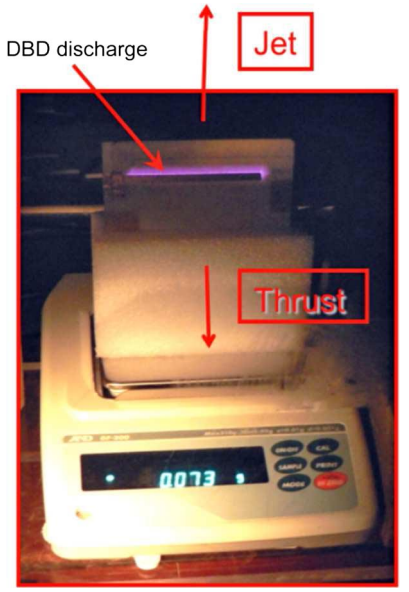

Fig. 3 Setup of an actuator on an analytic balance.

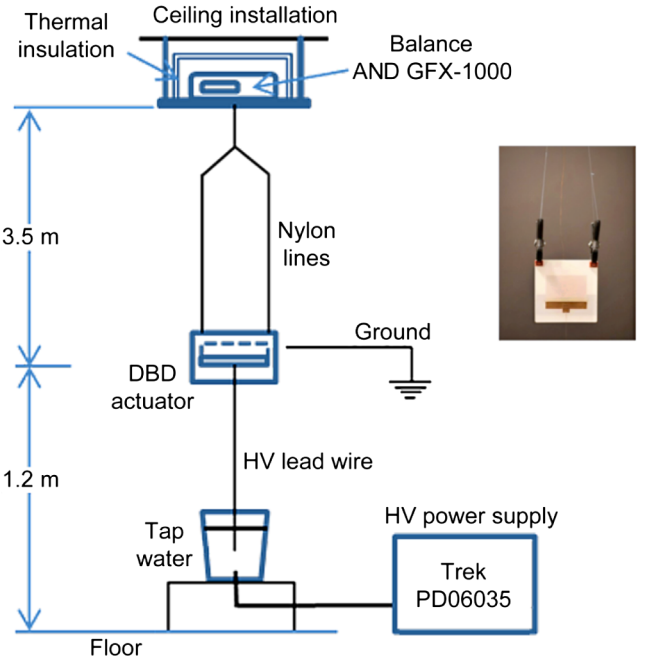

Fig. 4 Suspended actuator test setup schematic (not to scale).

actuator flowfield, and they can be used to calculate the wall shear force from the velocity field. For example, calculations from phase-averaged PIV data by Benard et al. ([16] Figs. 3c and 4c) and Kuhnhenn et al. ([17] Figs. 3 and 4c) showed that spatially averaged viscous terms are fairly constant in time and are localized in a thin sublayer above the surface, but they did not provide time-averaged values. Kriegseis et al. [18] calculations using PIV data showed the wall shear force increasing with distance from the exposed electrode to be up to 20% of the body force at end of the domain. We have not found other information in the literature on the wall shear force derived from PIV or LDA data. In our opinion, care is warranted using these results because the calculations use flowfield values near the surface, where LDA and PIV methods have limitations on accuracy, especially when surface charges are present and may affect the seeding particles. The cited authors do not provide specific information on the accuracy near the surface.

In light of the incomplete information, it is not yet possible to draw firm conclusions on the magnitude of the averaged wall shear force F_s relative to the averaged plasma body forces F_p, and we leave

clarifying this issue to a separate investigation. It has to be accepted at this point that the wall shear force F_s is not likely to be negligible and it cannot be isolated from the thrust measurement T_x. It is not necessarily a drawback because induced local shear stresses will accompany the volume force as input to interaction with the flow. The wall shear force is a result of the induced wall jet (larger shear forces with increased wall-jet velocity) and, together with the body force, it serves as part of the thrust, which is the performance figure of merit.

Note that we have used a steady (time-averaged) integral volume representation; however, the spatiotemporal momentum distribution is also of interest, and it may be especially important in certain flow control applications: for example, suppression of Tollmien–Schlichting instability waves (e.g., Grundmann and Tropea [19]). The time dependence of the plasma body force was a subject of extensive research and controversy. With sinusoidal applied voltage, Enloe et al. [20] identified different contributions from the forward stroke (the negative-going half-cycle glow discharge regime) and the backward stroke (the positive-going half-cycle streamer discharge regime). Although it was agreed that the forward stroke net force was positive ("push" mechanism, or force in the direction of the induced wall jet) and contributed to most of the body force, the direction of the backward stroke net force was controversial ("pull" or "push"?). Further experimental work by Enloe et al. [21], complemented by numerical simulations by Font et al. [22], identified the role of wall shear presented as induced drag and supported the "push–push" scenario. However, calculations based on flowfield measurements with PIV by Debien et al. [23,24] and Neumann et al. [25] supported the "push–pull" scenario, but it was later disproved by Benard et al. [16] calculations that supported push–push. It was contradicted in recent work by Kuhnhenn et al. [17], identifying a push–pull scenario. The wall shear stresses were found to play a role in the "dark" periods between discharge regimes and, according to Benard et al. [16], a push–pull mechanism exists if shear stresses are not taken into account. In addition, Kuhnhenn et al. [17] identified a frequency dependency of time lag between discharge and force initiations that may affect conclusions regarding the net force dynamics. It seems that calculated results depend on the manner shear stresses, and forces are accounted for in the calculations during the active discharges and the dark periods. Our conclusion is that the temporal force dynamics issue has not yet been completely resolved and further research is needed to clarify it.

Another approach to calculate the thrust or the body force is to measure the time-averaged wall jet using a pitot probe along the control volume inflow and outflow planes, as well as to calculate the thrust from the momentum equation applied to the control volume (e.g., [11,12]). The shortcomings in the latter approach are that it is an intrusive method, the probe is large relative to the wall-jet thickness, metallic probes will arc to the surface, and custom-made dielectric (e.g., glass) probes may accumulate static charge that may affect the flow in the vicinity. Pressure transducers appropriate to measure low velocities, at least down to 0.5 m/s to resolve the wall-jet profile, are also needed. Hot-wire anemometry can also be used [26–28], but the probe cannot get close to the discharge region. For completion, we mention that other methods to derive the thrust without flow measurements were used, and they included a pendulum deflection [20,29] and torsional pendulum [21]. Actuator performance was also characterized optically [30,31] and acoustically [32].

The preceding discussion was not intended to be comprehensive, and further information on the topic of body forces in DBD actuators can be found in the review articles by Benard and Moreau ([5] secs. 2.5–2.10) and Kotsonis ([6] sec. 2.2). An overview of several approaches used in derivation of the thrust from momentum equation terms was included in the work of Kriegseis et al. ([18] sec. III).

In contrast to the effort and constraints of the other various approaches, the direct measurement of thrust using a force balance is straightforward. When the actuator is placed on a force balance with the induced jet facing upward, the reading of the balance is the thrust of the actuator. The force balance can be a load cell or an analytic balance. Because load cells with the required resolution, range, and tare weight capacity are hard to find or nonexistent, an analytical balance is useful for this purpose (Fig. 3). It is desirable to use one with milligram resolution.

In summary, thrust (as measured by a force balance) is accepted by the research community as a good metric for determining AC-DBD actuator aerodynamic performance, despite the fact that the wall shear force is included. It is a simple, low-cost, convenient, and practical approach that allows quick measurements and performance comparisons of a large number of actuators. The objective is characterization of the overall aerodynamic performance of the actuator; therefore, the specific spatiotemporal behavior is not of interest. It is understood that the thrust indicates the plasma body force reduced by the wall shear force. The thrust is equal to the net momentum leaving the control volume, and inclusion of the wall shear force is not always a disadvantage.

III. Consistency of Thrust Measurements

We initially performed thrust measurements with various actuators held with acrylic fixtures in an acrylic enclosure. The balances used were A & D Company, Ltd. (AND, Japan) models GF-300 and GF-1000. This balance displayed good immunity to electromagnetic interference (EMI). It was placed inside a copper Faraday cage as an extra measure. A copper ground plane underneath was also used for appropriate grounding.

In the course of the tests, performed with acrylic and alumina dielectric actuators, we observed several problems. Durscher and Roy [13] also reported several open problems and areas that needed further investigation associated with actuators' thrust measurements reported in the literature. In our testing, we found large degrees of nonrepeatability, fluctuations, and drift in time. There was also strong dependence on the actuator conditioning profile ("burn-in"). This was also observed by other researchers (e.g., [11,13,33]). There was dependence on the manner of applying the voltage. For example, if the voltage was increased at a fixed frequency, the readings were different if the voltage was increased from one measuring point to the next, or if it was brought to zero between the measurement points. Also, when the high-voltage lead wire was charged, it was performing oscillatory motions, indicating dynamic forces; significant amplitudes of several inches of translation were observed with some setups.

There were indications that the measured thrust was affected by several phenomena. There was apparent interaction of the actuator with the enclosure, nearby objects, and the ground plane. Charges also appeared on the outside surface of the protective acrylic enclosure. The actuator dielectric itself exhibited charges that appeared to originate by remnant polarization, ferroelectric activation, and possible paraelectric behavior.

Finally, there was strong dependence on humidity. The effect is well known in the atmospheric pressure plasma research community (see, for example, the work of Koo et al. [34]), attributing the effect on changes in the plasma chemistry caused by generation of hydroxide (OH) radicals via interaction of electrons and the water molecules. A comprehensive study on the effect of humidity on the wall-jet velocity was performed by Benard et al. [35]. They performed experiments with relative humidity from 40 to 98% and showed that the wall-jet peak velocity decreased with increased humidity. Wilkinson et al. [36] found an increase or decrease in thrust with humidity, depending on the dielectric material used. They attributed some of the effect to water absorption in the dielectric. Further study on the effect of humidity was done by Wicks and Thomas [37]; they found a strong thrust reduction above 40% relative humidity. Regardless of these observations, when reviewing publications reporting experiments on DBD actuator performance, we found that humidity conditions were rarely reported.

External circuit parameters are also a factor in actuator performance [38]. In the work reported here, we have not made any changes affecting the external circuit impedance. The same power supply, supply cabling, and feed wires were used. The only impedance change between different tests was the impedance of the actuator test article and the impedance change caused by frequency dependence.

A more detailed description of issues encountered with thrust measurements can be found in [39]. The various issues need to be

further investigated and substantiated with an appropriate test setup and testing strategies.

Our experience with our attempts to accomplish consistent and reliable thrust measurements and the problems described previously led us to develop a new test setup and a new methodology for thrust measurement. Our methodology enabled the detection of negative thrust at low frequencies and resulted in the proposed antithrust hypothesis used to separate the relevant plasma thrust from the total measured thrust. These approaches will be described in the following.

IV. Test Setup

We have developed a test setup to counter some of the problems associated with our testing in an enclosure. The new test setup is shown in Fig. 4. The AND analytic balance we used (model GX-1000) had a linear accuracy of ± 3 mg and a repeatability of 1 mg. It was equipped with an underhook that enabled it to measure hanging loads. The balance was installed on a small aluminum platform attached to the laboratory ceiling. The balance was thermally insulated with an enclosure made from polystyrene foam sheets to minimize thermal drift. The air temperature in the enclosure was monitored with a thermocouple. The actuator test article was suspended with thin nylon monofilaments (fishing line) attached to a metal frame that was hung on the balance's hook. The test article was installed as far as practical from nearby objects. The floor underneath the test article consisted of grounded metal plates. The surrounding objects included metal cabinets, workbenches, metal and acrylic structures, and cement walls and floors with embedded steel reinforcing. The balance was installed about 3.5 m above the actuator. Testing revealed there was no detectable EMI interference by the balance due to the actuator. The nearest distance to adjacent objects from the actuator was 1.2 m. Typically, the distances were in the range of 1.5 to 2.0 m. The actuator was suspended about 1.2 m above the floor.

We used a Trek, Inc., high-voltage amplifier: model PD06035-L. Its maximum slew rate is 725 $\mathrm{V}/\mu\mathrm{s}$ (at no load, 10 to 90% typical). The dc gain is 3000 V/V. The effective slew rate was reduced to 245 $\mathrm{V}/\mu\mathrm{s}$ after the electrical actuator load was applied. The range of its working frequencies started at dc. The combination of its frequency and voltage output range was limited by the slew rate (and the load impedance). The sinusoidal input waveform was supplied with a synthesized signal generator from Stanford Research Systems (model DS345m). The Trek amplifier was equipped with a variable-intensity indicator to warn of output waveform distortion. We also simultaneously used an oscilloscope to detect output voltage distortion.

We used the factory-supplied output cable (Trek part number 43466B), with a total length of approximately 2 m. A section of the cable, approximately 1.5 m long, was routed through 1 in. internal diameter acrylic and PTFE (Polytetrafluoroethylene) tubes for extra insulation 10 cm above the metal floor. This arrangement was kept constant at the various tests so as not to vary the capacitance between the cable and the surroundings.

The high voltage was fed to the powered actuator electrode through a force-decoupling interface arrangement as follows. The high-voltage 28 AWG (American wire gauge) copper feed-wire lead from the actuator was suspended vertically with a metal counterweight into a styrene cup containing tap water that submerged the counterweight completely below the surface. The high voltage was fed from the output cable of the power supply into the water via a stainless-steel needle that pierced the bottom of cup. Sufficiently ionized tap water was selected due to its conductivity and allowed charging of the actuator electrode with minimal impedance. Dynamic forces caused by the lead wire, observed before with different setups, were minimized below detectable levels. The ground 28 AWG copper feed-wire lead was connected to the actuator covered electrode via a thinner 40 AWG copper wire suspended in an approximate catenary shape to minimize forces.

The high voltage was measured with the Trek built-in voltage monitor (3000:1 ratio). It was based on a high-performance voltage divider. It adequately represented the ac voltage on the electrodes within the moderate frequency ranges used. The built-in current monitor was not used for data, as our tests showed unsatisfactory high-frequency dynamic response. We have not recorded the current, as it was not within the objectives of this project.

We used a Nikon digital camera (model D300S) to take still images of the discharges. The camera settings of the images shown herein were F2.8, International Organization for Standardization (ISO) 200, with exposures of 30 s or as noted. A darkened room was required.

The balance readings were recorded using a LabVIEW (National Instruments) application. The balance provided continuously averaged load measurements 10 times per second. Testing performed on the balance revealed that this averaging occurred for time-varying loads at frequencies above 2 Hz. Alternatively, time-accurate readings could be acquired for loads that varied below 0.5 Hz. The accuracy of the AND balance was accomplished via a servo loop, activating an electromagnetic coil that maintained the deflection of the internal beam at zero. The electrical current to the coil was nearly linear with the load. This construction had a particular advantage relevant to our tests, as the static forces of the lead wires were null because there was no steady-state deflection that would cause stress forces in the lead wires.

The actuators used in the study reported here were made of 6.3 mm (0.25 in.) high-density polyethylene (HDPE) dielectric. The dielectric properties (see the Appendix) were close to those of PTFE (dielectric constant of $\varepsilon = 2.3$), making it a low-capacitance class of actuators that were proposed by the Notre Dame University group and shown to allow application of high voltage to achieve high levels of thrust [40]. We found that this material did not exhibit the sudden pinhole-type burnthrough that we encountered while using PTFE, PEEK (Polyether ether ketone), and other polymers. The HDPE exhibited excellent durability over long periods of time. The dimensions and other construction details of the actuators used are listed in the Appendix.

The ambient humidity, temperature, and pressure were measured with a combination probe and a recorder: Omega (Newport) model no. iServer Micorserver iBTHX-W-5. There was no attempt made to control the ambient humidity. It was set by the weather and the conditions in the building. The HVAC system controlled the room temperature but not the humidity. The humidity was constant over a particular test's time intervals.

V. Thrust Measurement Methodology

Usually, there is a need to perform a large number of thrust measurements within a test matrix indexed by frequency and voltage. We need to minimize the testing time while considering the issues described previously and take steps to obtain consistent results. To acquire the two-dimensional thrust data matrix, data must be acquired at constant voltage or at constant frequency. Because we have more experience with the magnitudes of thrust errors that are dependent upon voltage than those due to frequency, we favor acquiring data by maintaining constant voltage. Thrust data must be averaged over time at each pair of voltage and frequency values.

We are also trying to avoid performing numerous repetitions that would lead to comprehensive statistical analyses. Repetitive tests may take long periods of time (several hours or several days) and changes may occur in the actuator. These can be due to changes in ambient conditions (humidity, temperature), chemical reactions with the surface, erosion of the electrodes and the dielectric, dielectric heating, changes in the adhesives used, moisture absorption, and potential net charge nonequilibrium. If tests are performed in a closed chamber, changes of the surrounding gas composition can occur by accumulation of plasma-generated ozone and other species. There are also questions as to what is the appropriate period of data recording time used to calculate the average thrust for each point in the voltage-frequency matrix.

We use a burn-in process before data acquisition to condition the actuator to minimize potential long-term voltage-dependent thrust error. Our process is to expose the dielectric and surfaces to the maximum absolute voltage as well as to the maximum voltage slew rate with a sufficient dwell time to instigate the initial change. This change occurs relatively quickly (typically 3 to 10 min). Once changed, the actuator zero-thrust reference remains stable for a longer

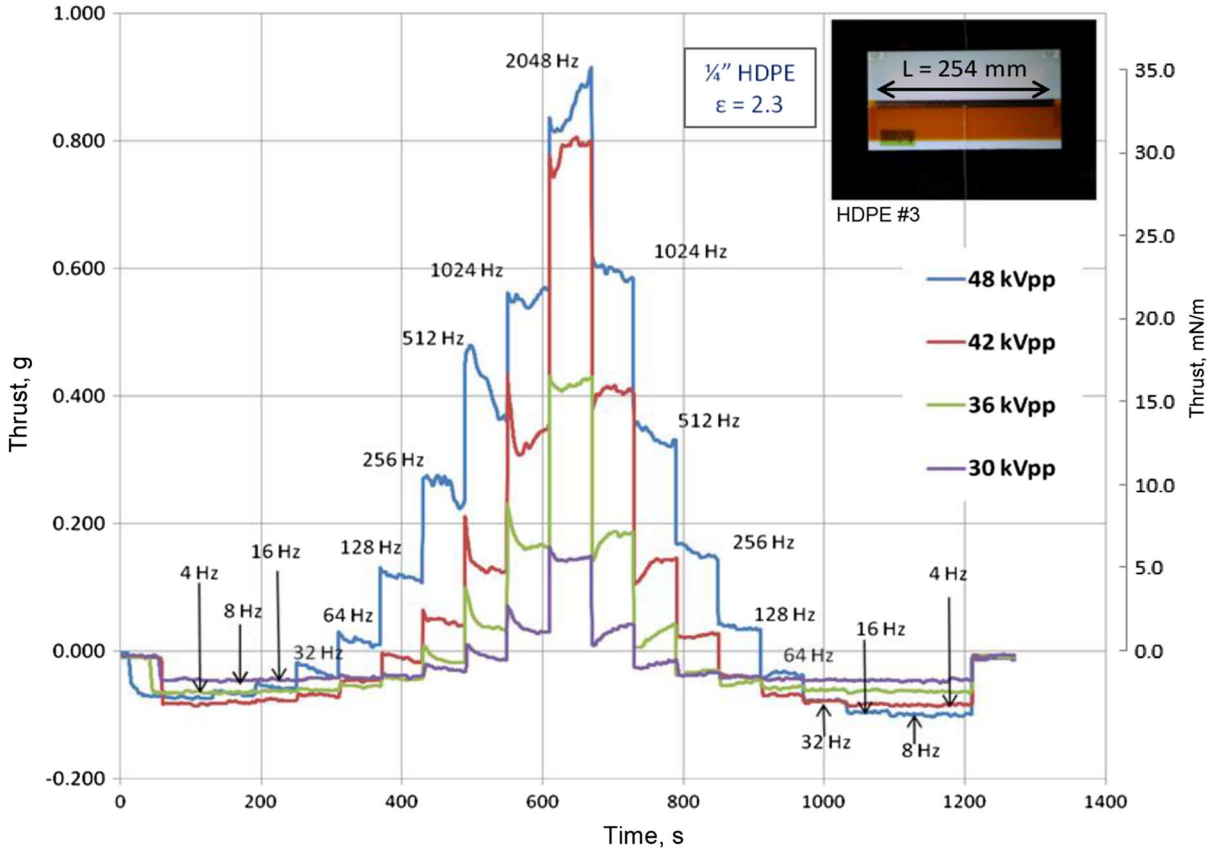

Fig. 5 Frequency sweeps at constant voltages: RH = 50%, dewpoint = 57°F. Sequence starts with 48 kV. Data taken after actuator idle for four days. (1 g equals 38.6 mN/m).

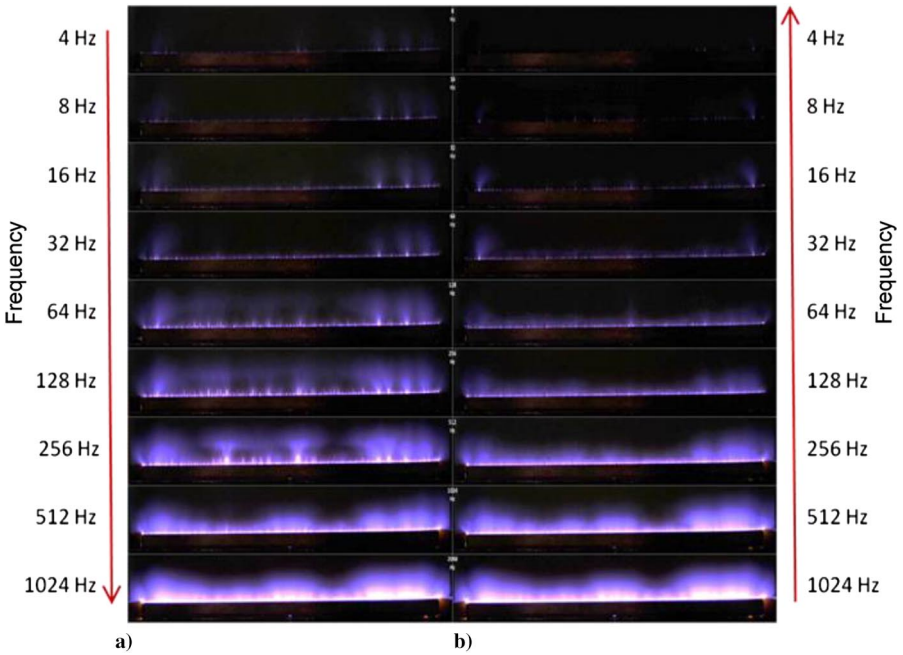

Fig. 6 Images of discharges corresponding to Fig. 5 48 kV_{p-p} frequency sweep.

period of time (2 to 3 h) that facilitates the long-term acquisition of the data matrix.

Based on our experience and extensive trials with different actuators, we developed a methodology of acquiring actuator thrust data using discrete frequency sweeps at constant voltages and recording average readings of the balance as follows.

First, the ranges of voltage and frequency of interest are determined. They are limited by the performance specifications of the power supply, which are mainly governed by its slew rate, the load impedance, and the breakdown voltage of the actuator dielectric. Next, the voltage is set to the highest voltage in the range, (48 kV_{p-p} in this example). The frequency is set to a low number (4 Hz) and then increased to the maximum frequency in the range (2048 Hz) in discrete frequency steps, with each lasting 60 s. The discrete frequencies are distributed in a logarithmic fashion with octave spacing. That is, each step is double the frequency of the prior step.

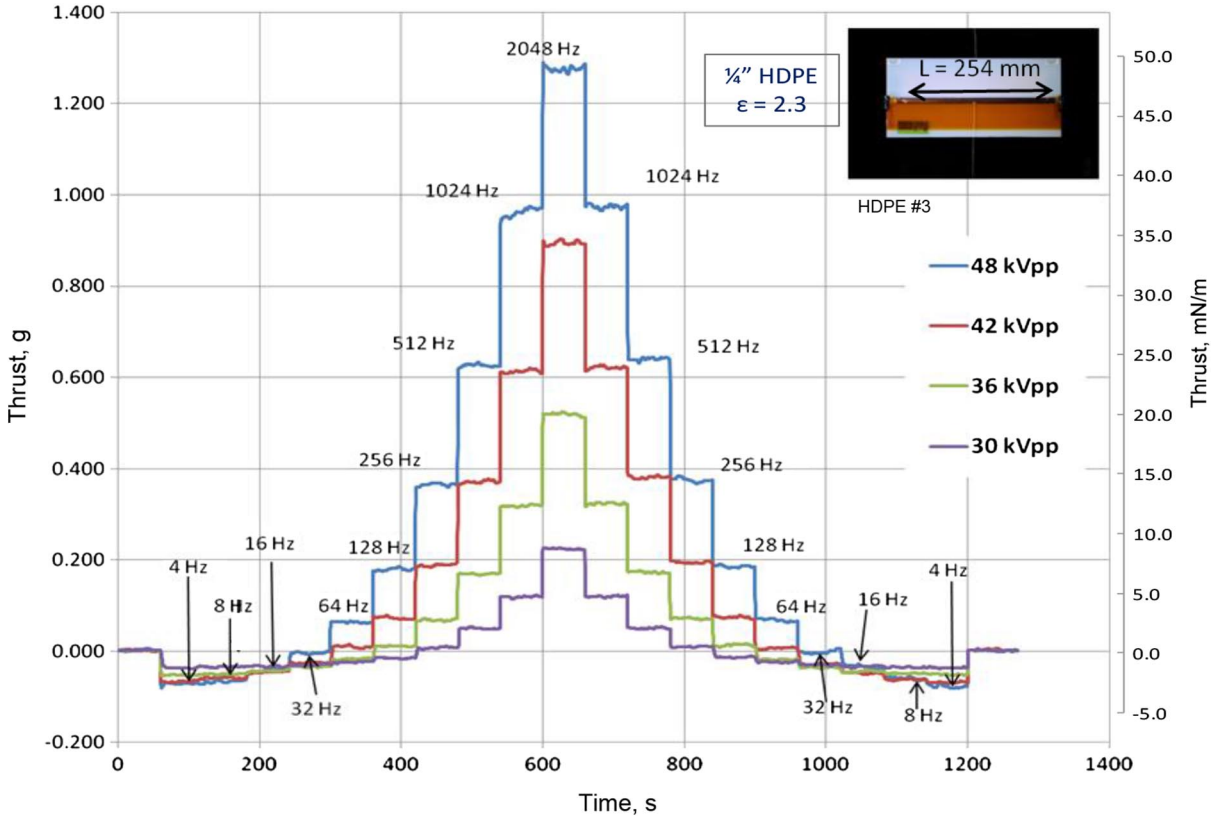

Fig. 7 Frequency sweeps at constant voltages: RH = 18%, dewpoint 33°F. Sequence starts with 48 kV_{p-p}. (1 g equals 38.6 mN/m).

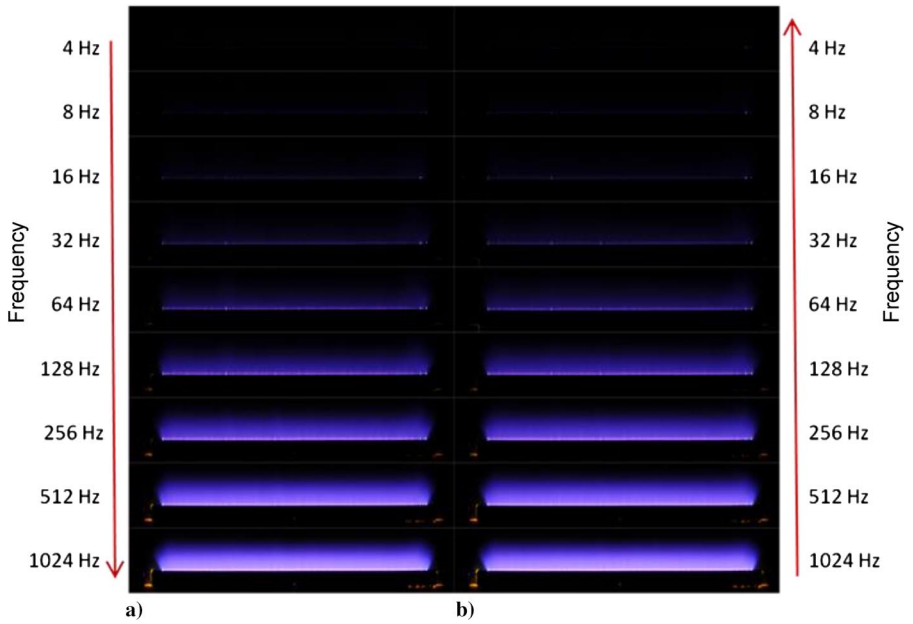

Fig. 8 Images of discharges corresponding to Fig. 7, 48 kV_{p-p} frequency sweep.

After the maximum frequency is reached, the process continues by decreasing the frequency down from the maximum frequency (2048 Hz) with the same discrete, 60 s steps, halving the frequency at each step down to the lowest frequency (4 Hz). That completes one fixed-voltage data series: a row in the matrix. The process is repeated at the next lower fixed voltage (42 kV_{p-p}). It is followed by repetitions at the other fixed voltages in the decreasing direction until the matrix is filled. We refer to this process as "frequency sweeps."

An example of frequency sweep raw data is shown in Fig. 5, showing thrust versus time for each fixed voltage. The actuator used is actuator HDPE 3 (Appendix). The relative humidity (RH) was 50%, and the correlated dew point was 57°F (averaged between four tests). The thrust data were collected after the actuator was inactive and unenergized for four consecutive days. The initial burn-in procedure was intentionally skipped in order to exhibit the need for one.

Examining Fig. 5, the first data row of the matrix, acquired at a constant 48 kV_{p-p}, clearly shows large asymmetry and hysteresis. Figure 6 reinforces this observation, as will be explained subsequently. This distortion and nonrepeatability are largely attributable to the lack of a prior burn-in. Further examination of Fig. 5 reveals that there is still mild asymmetry between the ascending and the descending halves of the other frequency sweeps, even after the first sweep at 48 kV_{p-p} provides a

partial burn-in. The thrust levels acquired at the same frequency and voltage differ instead of matching. The levels appear to depend on the frequency change direction. Furthermore, the small timescale thrust fluctuations are different. The 48 kV_{p-p} curve is distinguished by stronger initial spikes and fluctuations as compared to those at subsequently lower constant voltages. The behavior of the thrust fluctuations in the descending frequency sweeps is generally smoother and more consistent than in the ascending sweeps. Therefore, the descending data are recommended for further processing (shown in a subsequent section).

We have accompanied our measurements with still images taken with a digital camera (10 s exposures), as shown in Fig. 6. Taken at the same frequency and voltage, they show differences in the discharge structure that depend on the direction of the frequency step change. Also, there are dark areas within the plasma region on both directions of the frequency sweep that we cannot explain. On the ascending frequency side, bright localized filaments are observed; however, they are absent from the descending side. It is possible that they disappeared after the partial burn-in process (during prior frequency steps at 48 kV_{p-p}) that conditioned the actuator surface and electrodes.

A different case is shown in Fig. 7. The test actuator is the same HDPE 3 as the former, but with additional insulation comprising several layers of Kapton (DuPont) tape[‡] and corona dope[§] used as filler on the side and back (upstream) edges of the exposed electrode. The added insulation was intended to suppress visible "parasitic" corona discharge at electrode corners with a very small radius. It was desired to minimize potential thrust activity from localized electrode sites so as to focus on the thrust from the linear actuator edge discharge alone. The ambient humidity was much drier as compared to the previous case: RH of 18%, and dew point of 33°F. There are marked differences in the results. The steps are more uniform, fluctuation levels are lower, and there is more symmetry between the ascending and descending parts. The images shown in Fig. 8 show a uniform discharge without observable differences between the ascending and the descending frequency parts. We notice that the dark areas within the plasma region observed in Fig. 6 disappeared. We attribute the differences mainly to the lower humidity level; this trend was confirmed by additional tests not reported here. The additional insulation contributes to reduced fluctuations and increased smoothness of the frequency-dependency curves.

The thrust data are extracted from the frequency sweeps by averaging the data within each 60 s step. We used a window smoothing function that generated a single averaged value of the thrust at each frequency step. The results are shown in Fig. 9 for the high-humidity case. The low humidity case is shown in Fig. 10.

There are differences in the thrust level. The thrust is higher at the low-humidity case. It is about 44% higher at 48 kV_{p-p} and 2048 Hz in the drier ambient humidity.

In the drier case, the thrust corresponding to the ascending and descending frequencies curves virtually coincide. In the more humid case, there are differences between the two. In particular, the curve at 48 kV_{p-p} is different during the ascending frequency curve than during the descending curve. The reason is that this particular ascending curve happened to be the first actuator energization after four days of inactivity. It served as an unforced burn-in process. It experienced time-varying thrust changes above the typical baseline during this initial burn-in until it reached the highest frequency.

Even though we have not shown the standard deviation here, it is obvious that it is much larger in the humid case by examining the frequency sweeps steps (Figs. 5 and 7).

VI. Antithrust

When examining the results of the frequency sweeps shown in Figs. 5 and 7, we notice that the thrust is negative in a low-frequency range between 4 and 32 Hz (even up to 64 Hz in other cases tested but not shown here). To investigate further, we took detailed measurements of thrust versus voltage at constant low frequencies,

[‡]3M Company, model no. 5413, 0.08 mm (3 mil) thick.
[§]MG Chemicals Company, category no. 4226-1L.

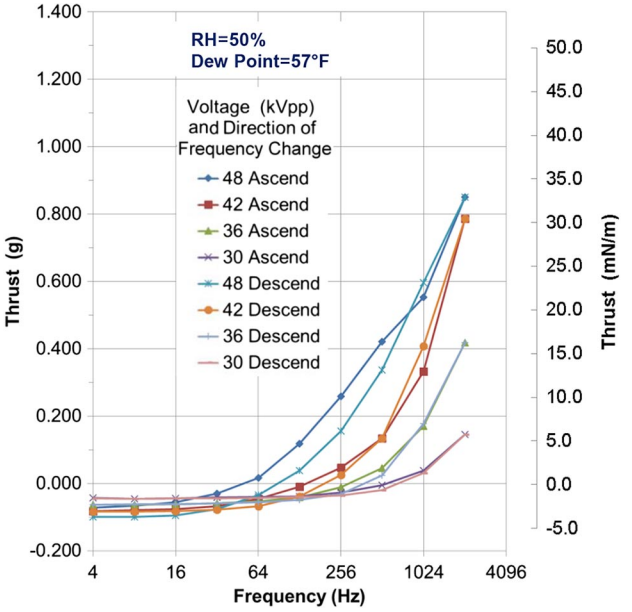

Fig. 9 Total thrust: Humid case. Corresponds to Fig. 5 (1 g equals 38.6 mN/m).

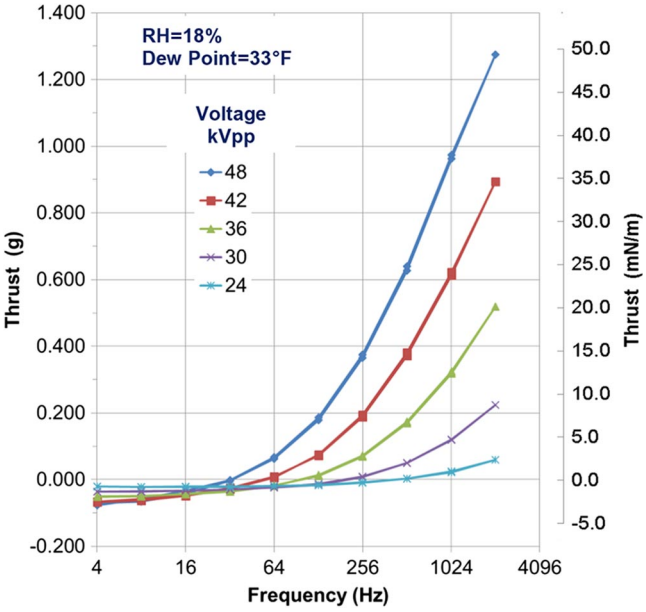

Fig. 10 Total thrust: Low-humidity case. Corresponds to Fig. 7. Note: ascending and descending trend overlap (1 g equals 38.6 mN/m).

shown in Fig. 11. The test actuator used was HDPE 2. The negative thrust values are noticeable. We examine the family of constant-frequency curves and notice that they appear to coincide with the lowest-frequency curve (64 Hz) at low voltages; then, they depart

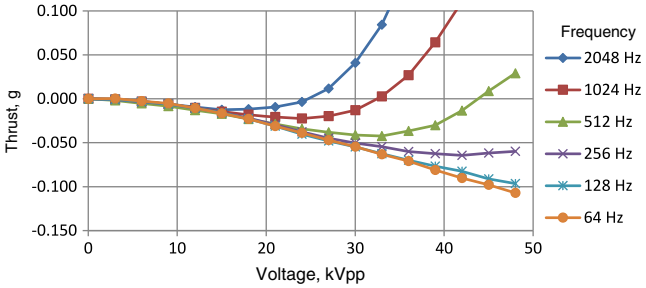

Fig. 11 Thrust as function of voltage at constant frequencies. Actuator HDPE 2. For this actuator, 100 mg equal 9.84 mN/m.

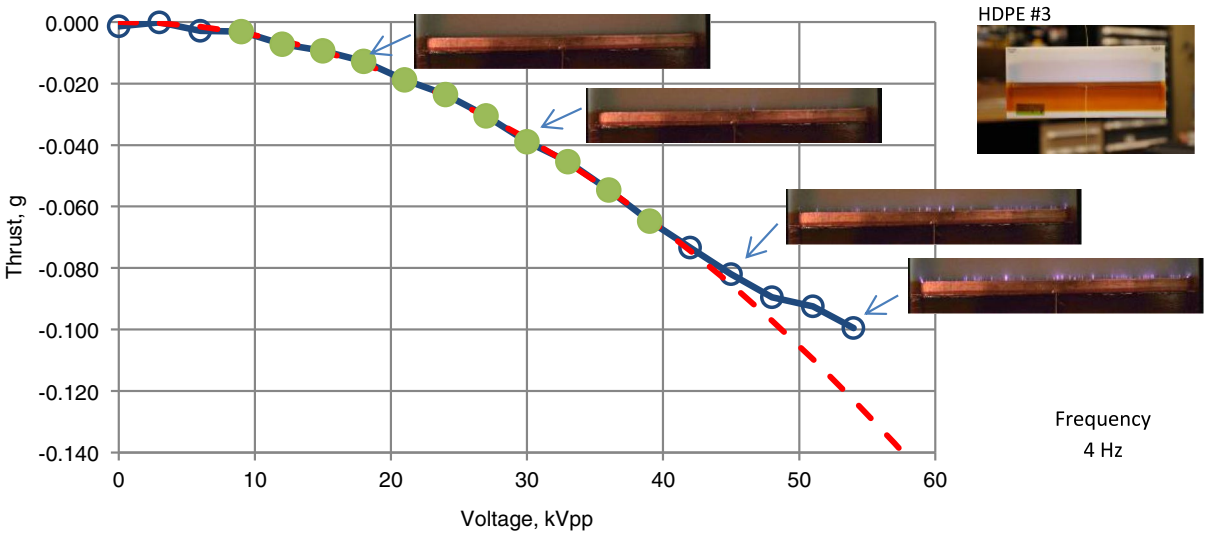

Fig. 12 Thrust as a function of voltage at constant frequency (4 Hz). Actuator HDPE 3. Images are enhanced, 30 s exposures. For this actuator, 100 mg equal 38.6 mN/m.

from that baseline with increasing voltage. The "departure" voltage for each curve appears to shift to the left to a lower voltage with each frequency increase. These observations motivated us to investigate if there was an ultimate lower-frequency limit curve. We have repeated the test at a constant frequency of 4 Hz for test actuator HDPE 3, shown in Fig. 12. We were able to easily fit a parabolic curve to most of the points while acknowledging there were other points that departed from the natural parabola. Enhanced digital still images of a 30 s exposure taken during the voltage sweep showed that there was corona or plasma discharges at the voltage points that departed from the parabolic baseline, whereas no discharges were observed at the lower-voltage points that fit well to the same parabolic curve. In additional tests on other test articles, we found that the parabolic curve could always be fit to the low-voltage range of averaged thrust values for low fixed frequencies when visible discharges were not present. The parabola was also found to be frequency independent.

These observations lead us to formulate a hypothesis as follows:

$$\text{Total Thrust} = \text{Plasma Thrust} + \text{Antithrust} \tag{2}$$

The total thrust is the thrust as measured by the balance. The plasma thrust is the thrust associated with the discharge on the exposed electrode that generates the momentum, and it includes the shear force term [Eq. (1)]. The second term on the right-hand side was named antithrust because it is always negative and is represented by the parabolic curve fit:

$$\text{Antithrust} = \text{kV}^2 \tag{3}$$

We have found by performing additional tests under different conditions that the parabolic antithrust is confirmed to be frequency independent at a minimum between 4 and 64 Hz.

We make the following assumptions:

1) The antithrust is frequency independent at any frequency.

2) The antithrust is only voltage dependent and can be extrapolated to higher voltages.

3) The antithrust is always present, even during visible plasma.

With these assumptions, the coefficient k in Eq. (3) is a frequency- and voltage-independent constant. We therefore can use the antithrust parabola to separate the plasma thrust from the total thrust. The plasma thrust is the quantity of interest for characterizing the aerodynamic performance of the actuator. The antithrust curve, or

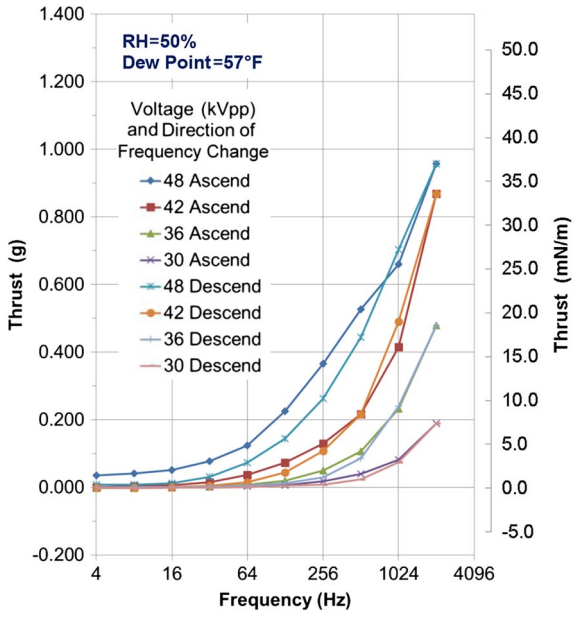

Fig. 13 Isolated plasma thrust: Humid case. Data of Fig. 9 corrected for anti-thrust (1 g equals 38.6 mN/m).

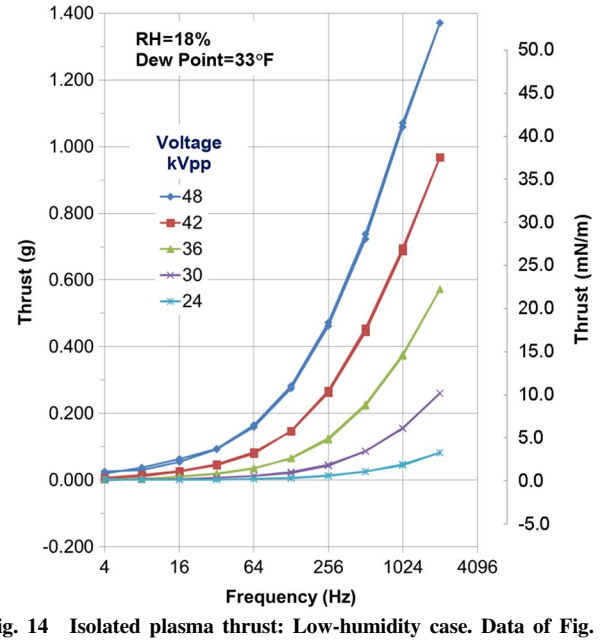

Fig. 14 Isolated plasma thrust: Low-humidity case. Data of Fig. 10 corrected for anti-thrust. Note: Ascending and descending trends overlap (1 g equals 38.6 mN/m).

the coefficient k, needs to be generated for each actuator and for each test installation by performing a voltage sweep at a low frequency (usually between 4 and 32 Hz in practice). It is very important to monitor the voltage waveform because even minor distortion will significantly affect antithrust.

We propose that the antithrust always exists, but is somewhat masked by the thrust from visible plasma discharges as the voltage and frequency increase. We also propose that it is an installation-dependent effect that depends on the actuator surroundings and its own geometrical and dielectric properties. The V^2 dependence is similar to the voltage dependence of electrostatic forces. However, at this stage of the research, we have no experimental or computational verification to support a statement that the antithrust is caused by only electrostatic forces. It does not seem to be related to shear forces because it appears before initiation of discharges that induce flow and the associated shear stresses. We also have attempted to study the dependence of the antithrust on humidity, but we did not yet have sufficient data for conclusive results.

As an example, we performed the antithrust correction on the thrust data of the two cases shown earlier in Figs. 9 and 10, and we isolated the plasma thrust. The results are shown in Figs. 13 and 14. Because a negative quantity was subtracted, the values of the plasma thrust increased relative to the measured thrust. This correction was substantial for smaller actuators and lower thrusts. We have found cases where the error could even exceed 100% if the correction was ignored.

The current approach was used in subsequent work [41] and enabled a new thrust–voltage relationship to be exposed, which differed than in prior work.

VII. Effect of the Test Installation

To demonstrate the dependence of antithrust on the test installation, we performed a test with a smaller actuator: HDPE 2 (see the Appendix). The results are shown in Fig. 15. We first performed the antithrust measurement at 32 Hz on the freely suspended actuator. The results are shown in blue in Fig. 15a. The antithrust parabola was fitted, and the deviation of the thrust from the parabola is noticeable starting at 30 kV_{p-p}.

We then placed a large-diameter seamless, conductive cylinder around the actuator [304 stainless steel, 16 in. diameter, 59 in. long, 0.0375 in. thick (20 gauge); McMaster-Carr Supply Company part number 2538K652]. The cylinder was suspended, so the actuator was located inside it, as shown in Fig. 15c. The cylinder was grounded and the antithrust measurements repeated (plotted in green). There is a marked difference between the unconfined actuator and the actuator installed within the grounded cylinder. The antithrust parabolic curves are different, the antithrust is larger with the grounded cylinder, and the thrust does not significantly deviate from the parabola. The measurements were repeated with the cylinder ungrounded, allowing its voltage potential to float. The results are plotted in red and are closer to the unconfined actuator case.

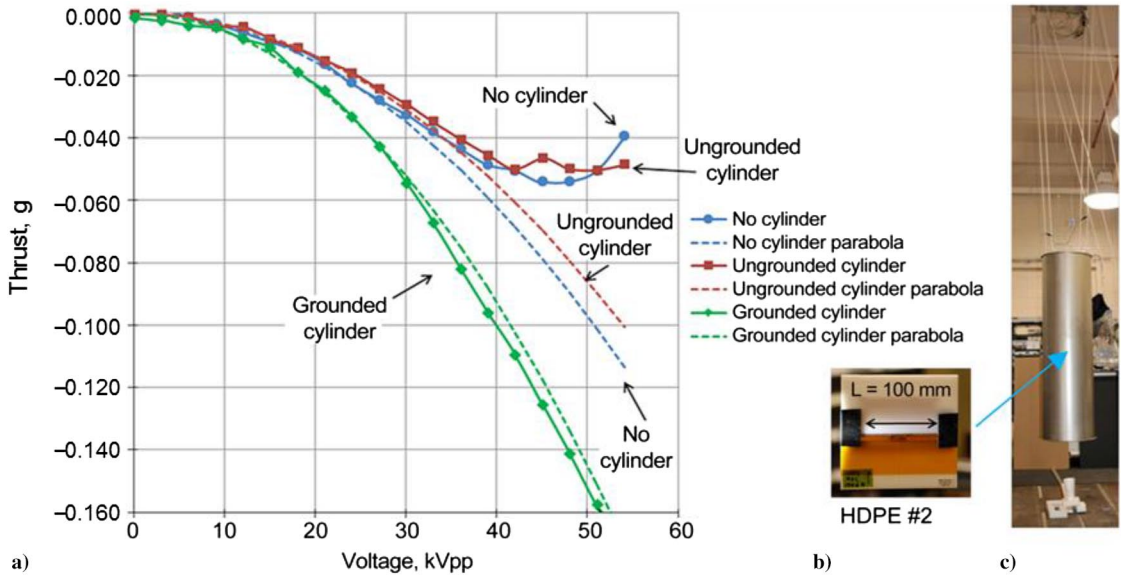

Fig. 15 Antithrust of an actuator within a surrounding cylinder. Dewpoint 60°F. a) Thrust as function voltage at fixed frequency (32 Hz), b) image of HDPE 6.3 mm-thick actuator; and c) image of the suspended metal cylinder experimental setup. Actuator is suspended inside cylinder at midlevel, as indicated by the arrow (0.100 g equals 9.84 mN/m).

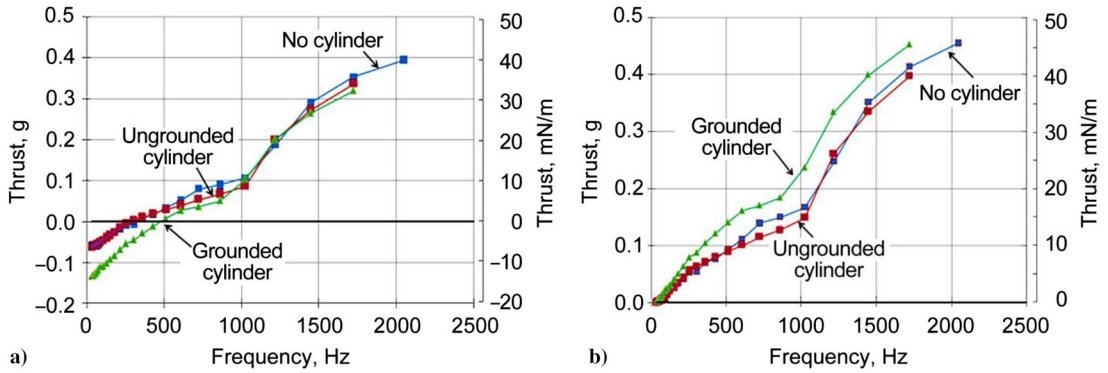

Fig. 16 Thrust as a function of frequency at a constant voltage (48 kV_{pp}). Actuator HDPE 2. a) Total thrust, b) plasma thrust after antithrust correction (0.1 g equals 9.84 mN/m).

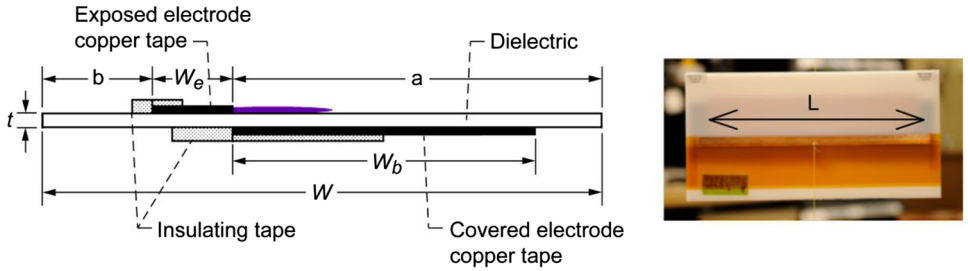

Fig. A1 DBD plasma actuator test article: geometry and dimensions.

Table A1 Actuators dimensions and information[a, b]

Designation	t	W_e	W_b	L	W	a	b	Thrust T to T/L conversion factor
Units	mm	mm	mm	mm	mm	mm	mm	g to mN/m
HDPE 2	6.3	9.8	48.2	100	152	78	64.2	98.3616
HDPE 3	6.3	9.8	49	254	151	75.5	65.1	38.6089

[a]Actuator geometries and materials are as shown in Fig. A1. Table A1 lists dimensions and conversion factor to convert from the thrust in grams to the normalized thrust (thrust per unit length of the exposed electrode) in millinewtons per meter.

[b]Due do fabrication inaccuracies, the sum $a + b + W_e$ does not equal W.

These experiments serve as a significant validation of our antithrust hypothesis that implies that the antithrust is installation dependent. It seems that the surrounding material affected the electrical field around the actuator, resulting in a different antithrust force.

Thrust measurements for the three cases are plotted in Fig. 16a as a function of frequency for a constant voltage of 48 kV_{p-p}. The negative thrust is observed at low frequencies. Above 1000 Hz, the three cases appear to be overlapping or having small differences, and we may be led to conclude that the actuator performance is identical within these three cases, regardless of the surrounding cylinder. However, when the antithrust correction is performed to isolate the plasma thrust (results shown in Fig. 16b), it shows that the grounded cylinder case has larger plasma thrust as compared to the open actuator case and that its performance is affected by the surrounding grounded sleeve.

VIII. Conclusions

The results shown were for pure sinusoidal waveforms in continuous-wave mode without pulsing or modulation. Some modifications and adaptations will be needed to evaluate other waveforms. This paper was not intended to provide comprehensive performance results of DBD actuators using thrust measurements; rather, it was intended to expose a few considerations that need to be taken in studies of the aerodynamic performance of these devices. The current study includes adopting a methodology to obtain consistent thrust results, defining an appropriate test setup, isolating the plasma force with our proposed antithrust hypothesis, and considering the effect of humidity. The effect of humidity on thrust is consistent with [35,37]. It is recommended to take extra care when comparing the thrust performance of actuators between different setups and laboratories.

In addition to the effect of the issues discussed in this project, it needs to be noted that there is variability in construction of the test articles. Most of the studies reported in the literature are performed with handmade actuators. There can be problems with insufficient insulation of sharp edges, the degree of variation in the fabrication, and the trapping of air bubbles within adhesives and between layers of dielectrics. The variability can accumulate to large error bars and make conclusions on the relative performance of actuators prone to significant uncertainties. An uncertainty analysis was not performed because it requires developing a strategy and a significant effort of collecting data from numerous actuators. The focus was placed on disseminating the new ideas, techniques, and results for discussion, evaluation, and verification by the research community. Uncertainty analysis is left for future work.

In future work, the source of the antithrust will be investigated and there will be an attempt to confirm the current hypothesis. It will likely be related to electrostatic forces between the actuator and the test installation. The electrostatic force field is a complex three-dimensional interaction that, in principle, can be calculated using numerical solution methods. Anticipated difficulties may be the accurate calculation of electrostatic fields caused by sharp edges and corners, as well as defining the electric potential and electric current of the surrounding objects. Bulk air charging unrelated to pure Coulombic electrostatic forces may also be investigated.

The dependence upon the installation indicates that the actuator performance in the aerodynamic flow control application in a flight vehicle or a propulsion system will depend on its neighboring geometry, materials, and electric potential. The surroundings will alter its performance. For example, if installed inside a jet engine, the actuator will be in very close proximity to grounded metallic surfaces: a situation that is different than when installed on an aircraft wing.

The inconsistent performance and the strong dependence on humidity have implications on the DBD actuator integration in a flow control system. If the actuator is installed as a component in an open control loop, there is less of a guarantee that the momentum it will provide will be as designed. A solution to this limitation may be inclusion of an active controller that will ensure it provides the desired momentum. Sufficient reserve power will be needed from the power supply. This problem does not exist when the actuator is incorporated in a closed control loop. The control loop will adjust the momentum it provides, but there will still be a requirement for a sufficient reserve margin of the power supply.

Appendix: Actuator Dimensions and Properties Information

The actutors dimensions are shown in Fig. A1 and in Table A1. The dielectric material, electrode material, and electrode insulation material used are listed in the following.

The dielectric material used was high-density polyethylene with a nominal thickness of 1/4 in. (McMaster–Carr part number 8619K461). The following were the HDPE electrical properties:[¶]

1) The dielectric constant was 2.3 at 1 kHz.
2) The dielectric strength was 22 MV/m.
3) The dissipation factor was 0.0005 at 1 kHz.

The electrodes material was copper tape with conductive adhesive (3M no. 1181), with the following properties:

[¶]Information may be found online at http://www.azom.com [retrieved 12 December 2013].

1) The copper thickness was 0.04 mm (1.4 mil).

2) The adhesive thickness was 0.03 mm (1.2 mil).

The electrode insulation materials were as follows:

1) The covered electrode edge was insulted with 3M Scotch-Seal no. 229 pads.

2) The exposed electrode was insulated with Kapton (E.I. du Pont de Nemours and Company) 3M no. 5413 that was 0.08 mm (3 mil) thick.

3) Super corona dope was also used, which was made by MG Chemicals, Inc. (category no. 4226-1L).

Acknowledgments

This project was supported by the National Aeronautics and Space Administration Transformational Tools and Technologies Project (formerly the Aerospace Sciences Project of the Fundamental Aeronautics Program).

References

[1] Moreau, E., "Airflow Control by Non-Thermal Plasma Actuators," *Journal of Physics, D: Applied Physics*, Vol. 40, No. 3, 2007, pp. 605–636.
doi:10.1088/0022-3727/40/3/S01

[2] Corke, T. C., Post, M. L., and Orlov, D. M., "SDBD Plasma Enhanced Aerodynamics: Concepts, Optimization and Applications," *Progress in Aerospace Sciences*, Vol. 43, Nos. 7–8, 2007, pp. 193–217.
doi:10.1016/j.paerosci.2007.06.001

[3] Corke, T. C., Post, M. L., and Orlov, D. M., "Single Dielectric Barrier Discharge Plasma Enhanced Aerodynamics: Physics, Modeling and Applications," *Experiments in Fluids*, Vol. 46, No. 1, 2009, pp. 1–26.
doi:10.1007/s00348-008-0582-5

[4] Corke, T. C., Enloe, C. L., and Wilkinson, S. P., "Dielectric Barrier Discharge Plasma Actuators for Flow Control," *Annual Reviews of Fluid Mechanics*, Vol. 42, No. 1, 2010, pp. 505–529.
doi:10.1146/annurev-fluid-121108-145550

[5] Benard, N., and Moreau, E., "Electrical and Mechanical Characteristics of Surface AC Dielectric Barrier Discharge Plasma Actuators Applied to Airflow Control," *Experiments in Fluids*, Vol. 55, No. 11, 2014, Paper 20141846.
doi:10.1007/s00348-014-1846-x

[6] Kotsonis, M., "Diagnostics for Characterisation of Plasma Actuators," *Measurement Science and Technology*, Vol. 26, No. 9, 2015, Paper 092001.
doi:10.1088/0957-0233/26/9/092001

[7] Kriegseis, J., Simon, B., and Grundmann, S., "Towards In-Flight Applications? A Review on Dielectric Barrier Discharge-Based Boundary-Layer Control," *Applied Mechanics Reviews*, Vol. 68, No. 2, 2016, Paper 020802.
doi:10.1115/1.4033570

[8] Roupassov, D. V., Nikipelov, A. A., Nudnova, M. M., and Starikovskii, A. Y., "Flow Separation Control by Plasma Actuator with Nanosecond Pulsed-Periodic Discharge," *AIAA Journal*, Vol. 47, No. 1, 2009, pp. 168–185.
doi:10.2514/1.38113

[9] Starikovskiy, A., Gordon, S., Post, M., and Miles, R., "Barrier Discharge Development and Thrust Generation at Low and High Pressure Conditions," AIAA Paper 2014-0329, Jan. 2014.
doi:10.2514/6.2014-0329

[10] Glezer, A., and Amitay, M., "Synthetic Jets," *Annual Reviews of Fluid Mechanics*, Vol. 34, No. 1, 2002, pp. 503–529.
doi:10.1146/annurev.fluid.34.090501.094913

[11] Hoskinson, A. R., Hershkowitz, N., and Ashpis, D. E., "Force Measurements of Single and Double Barrier DBD Plasma Actuators in Quiescent Air," *Journal of Physics, D: Applied Physics*, Vol. 41, No. 24, 2008, Paper 245209.
doi:10.1088/0022-3727/41/24/245209

[12] Baughn, J. W., Porter, C. O., Peterson, B. L., McLaughlin, T. E., Enloe, C. L., Font, G. I., and Baird, C., "Momentum Transfer for an Aerodynamic Plasma Actuator with an Imposed Boundary Layer," AIAA Paper 2006-0168, 2006.
doi:10.2514/6.2006-168

[13] Durscher, R., and Roy, S., "Evaluation of Thrust Measurement Techniques for Dielectric Barrier Discharge Actuators," *Experiments in Fluids*, Vol. 53, No. 4, 2012, pp. 1165–1176.
doi:10.1007/s00348-012-1349-6.

[14] Opaits, D. F., Likhanskii, A., Edwards, M., Zaidi, S., Shneider, M., Macheret, S., and Miles, R., "Surface Plasma Induced Wall Jets," AIAA Paper 2010-0469, Jan. 2010.
doi:10.2514/6.2010-469

[15] Glauert, M. B., "The Wall Jet," *Journal of Fluid Mechanics*, Vol. 1, No. 6, 1956, pp. 625–643.
doi:10.1017/S002211205600041X

[16] Benard, N., Debien, A., and Moreau, E., "Time-Dependent Volume Force Produced by a Non-Thermal Plasma Actuator from Experimental Velocity Field," *Journal of Physics, D: Applied Physics*, Vol. 46, No. 24, 2013, Paper 245201.
doi:10.1088/0022-3727/46/24/245201

[17] Kuhnhenn, M., Simon, B., Maden, I., and Kriegseis, J., "Interrelation of Phase-Averaged Volume Force and Capacitance of Dielectric Barrier Discharge Plasma Actuators," *Journal of Fluid Mechanics*, Vol. 809, Dec. 2016, Paper R1.
doi:10.1017/jfm.2016.679

[18] Kriegseis, J., Schwarz, C., Tropea, C., and Grundmann, S., "Velocity-Information-Based Force-Term Estimation of Dielectric-Barrier Discharge Plasma Actuators," *Journal of Physics, D: Applied Physics*, Vol. 46, No. 5, 2013, Paper 055202.
doi:10.1088/0022-3727/46/5/055202

[19] Grundmann, S., and Tropea, C., "Active Cancellation of Artificially Introduced Tollmien–Schlichting Waves Using Plasma Actuators," *Experiments in Fluids*, Vol. 44, No. 5, 2008, pp. 795–806.
doi:10.1007/s00348-007-0436-6

[20] Enloe, C. L., McHarg, M. G., and McLaughlin, T. E., "Time-Correlated Force Production Measurements of the Dielectric Barrier Discharge Plasma Aerodynamic Actuator," *Journal of Applied Physics*, Vol. 103, No. 7, 2008, Paper 073302.
doi:10.1063/1.2896590

[21] Enloe, C., McHarg, M., Font, G., and McLaughlin, T., "Plasma-Induced Force and Self-Induced Drag in the Dielectric Barrier Discharge Aerodynamic Plasma Actuator," AIAA Paper 2009-1622, Jan. 2009.
doi:10.2514/6.2009-1622

[22] Font, G. I., Enloe, C. L., and McLaughlin, T. E., "Plasma Volumetric Effects on the Force Production of a Plasma Actuator," *AIAA Journal*, Vol. 48, No. 9, 2010, pp. 1869–1874.
doi: 10.2514/1.J050003

[23] Debien, A., Benard, N., David, L., and Moreau, E., "Unsteady Aspect of the Electrohydrodynamic Force Produced by Surface Dielectric Barrier Discharge Actuators," *Applied Physics Letters*, Vol. 100, No. 1, 2012, Paper 013901.
doi:10.1063/1.3674308

[24] Debien, A., Benard, N., David, L., and Moreau, E., "Erratum: 'Unsteady Aspect of the Electrohydrodynamic Force Produced by Surface Dielectric Barrier Discharge Actuators' [Appl. Phys. Lett. 100, 013901 (2012)]," *Applied Physics Letters*, Vol. 101, No. 22, 2012, Paper 229903.
doi:10.1063/1.4767989

[25] Neumann, M., Friedrich, C., Czarske, J., Kriegseis, J., and Grundmann, S., "Determination of the Phase-Resolved Body Force Produced by a Dielectric Barrier Discharge Plasma Actuator," *Journal of Physics, D: Applied Physics*, Vol. 46, No. 4, 2013, Paper 042001.
doi:10.1088/0022-3727/46/4/042001

[26] Corke, T., and Matlis, E., "Phased Plasma Arrays for Unsteady Flow Control," AIAA Paper 2000-2323, June 2000.
doi:10.2514/6.2000-2323

[27] Corke, T. C., Cavalieri, D. A., and Matlis, E., "Boundary-Layer Instability on Sharp Cone at Mach 3.5 with Controlled Input," *AIAA Journal*, Vol. 40, No. 5, 2002, pp. 1015–1018.
doi:10.2514/2.1744

[28] Hultgren, L. S., and Ashpis, D. E., "Demonstration of Separation Delay with Glow Discharge Plasma Actuators," AIAA Paper 2003-1025, Jan. 2003.
doi:10.2514/6.2003-1025

[29] Emanuel, M., Bristow, D., and Rovey, J., "Force Sensing of an Asymmetric Dielectric Barrier Discharge Using Mechanical Resonators," AIAA Paper 2012-0409, Jan. 2012.
doi:10.2514/6.2012-409

[30] Enloe, C. L., McLaughlin, T. E., Van Dyken, R. D., Kachner, K. D., Jumper, E. J., and Corke, T. C., "Mechanisms and Responses of a Single Dielectric Barrier Plasma Actuator: Plasma Morphology," *AIAA Journal*, Vol. 42, No. 3, 2004, pp. 589–594.
doi:10.2514/1.2305

[31] Enloe, C. L., McLaughlin, T. E., Van Dyken, R. D., Kachner, K. D., Jumper, E. J., Corke, T. C., and Haddad, O., "Mechanisms and Responses of a Dielectric Barrier Plasma Actuator: Geometric Effects,"

AIAA Journal, Vol. 42, No. 3, 2004, pp. 595–604.
doi:10.2514/1.3884

[32] Baird, C., Enloe, C., McLaughlin, T., and Baughn, J., "Acoustic Testing of the Dielectric Barrier Discharge (DBD) Plasma Actuator," AIAA Paper 2005-0565, Jan. 2005.
doi:10.2514/6.2005-565

[33] Ferry, J., and Rovey, J., "Thrust Measurement of Dielectric Barrier Discharge Plasma Actuators and Power Requirements for Aerodynamic Control," AIAA Paper 2010-4982, June 2010.
doi:10.2514/6.2010-4982

[34] Koo, I. G., Cho, J. H., and Lee, W. M., "Influence of Gas Humidity on the Uniformity of RF-Powered Atmospheric-Pressure Low-Temperature DBD Plasmas," *Plasma Processes and Polymers*, Vol. 5, No. 2, 2008, pp. 161–167.
doi:10.1002/(ISSN)1612-8869

[35] Benard, N., Balcon, N., and Moreau, E., "Electric Wind Produced by a Surface Dielectric Barrier Discharge Operating over a Wide Range of Relative Humidity," AIAA Paper 2009-0488, Jan. 2009.
doi:10.2514/6.2009-488

[36] Wilkinson, S., Siochi, E., Sauti, G., Xu, T.-B., Meador, M. A., and Guo, H., "Evaluation of Dielectric-Barrier-Discharge Actuator Substrate Materials," AIAA Paper 2014-2810, June 2014.
doi:10.2514/6.2014-2810

[37] Wicks, M., and Thomas, F. O., "Effect of Relative Humidity on Dielectric Barrier Discharge Plasma Actuator Body Force," *AIAA Journal*, Vol. 53, No. 9, 2015, pp. 2801–2805.
doi:10.2514/1.J053810

[38] Farouk, T., Farouk, B., Gutsol, A., and Fridman, A., "Atmospheric Pressure Radio Frequency Glow Discharges in Argon: Effects of External Matching Circuit Parameters," *Plasma Sources Science and Technology*, Vol. 17, July 2008, Paper 035015.
doi:10.1088/0963-0252/17/3/035015

[39] Ashpis, D. E., and Laun, M. C., "Dielectric Barrier Discharge (DBD) Plasma Actuators Thrust—Measurement Methodology Incorporating New Anti-Thrust Hypothesis," AIAA Paper 2014-0486, Jan. 2014; also NASA TM-2014-218115, July 2014.
doi:10.2514/6.2014-0486

[40] Thomas, F. O., Corke, T. C., Iqbal, M., Kozlov, A., and Schatzman, D., "Optimization of Dielectric Barrier Discharge Plasma Actuators for Active Aerodynamic Flow Control," *AIAA Journal*, Vol. 47, No. 9, 2009, pp. 2169–2178.
doi:10.2514/1.41588

[41] Ashpis, D. E., and Laun, M. C., "Characterization of DBD Plasma Actuators Performance Without External Flow—Part I: Thrust-Voltage Quadratic Relationship in Logarithmic Space for Sinusoidal Excitation," AIAA Paper 2016-4013, June 2016.
doi:10.2514/6.2016-4013